scientific reports

Check for updates

OPEN

Fabrication of a novel 3D-printed perfusion bioreactor for complex cell culture models

Brian H. Jun[1], Jacob E. Torrez[1], David J. Ross[2], Brian M. Patterson[2], Mohammad O. Ishak[3], Arasely M. Rodriguez[4], Jennifer F. Harris[5] & Katie L. Davis-Anderson[1]✉

We introduce a novel fabrication method for developing a 3D-printed perfusion bioreactor (3D-PBR) to facilitate the in situ growth and differentiation of human bone marrow (BM)-derived mesenchymal stem cells (MSCs) while enabling coculture with vascular cells. To recapitulate human physiology, in vitro platforms must incorporate several key features of their native target organ. This often entails a supportive 3D architecture for growing and differentiating multiple human cell types in situ under perfusion. Other essential characteristics include reproducibility, ease of customization, and biocompatibility. Our 3D-PBR combines these features and was fabricated using a biocompatible resin-based polymer, which was 3D-printed, followed by the addition of a permeable membrane to create a coculture microenvironment. MSCs were encapsulated in a collagen-fibrin gel alongside human endothelium within the 3D-PBR. The physical cues that our 3D-PBR provided facilitated the differentiation of MSCs into specific lineages, such as adipocytes and osteoblasts. Immunohistochemistry images demonstrated that cells grown in the 3D-PBR exhibited more physiologically relevant BM perivascular niche markers compared to static culture models. Our method utilizes emerging 3D printing techniques and alternative materials, departing from traditional PDMS-based soft lithography. These advancements in fabrication further enhance in vitro platforms for diverse cell culture models and vascular permeability assays.

In recent decades, significant advancements in microphysiological systems (MPS), also known as organ-on-a-chip, have enabled the development of various tissue and organ models in microfluidic platforms[1,2]. The most commonly used design, which can be fabricated in-house or purchased commercially, consists of two compartments connected by a porous barrier. This design allows for culturing different cell types or tissues while enabling biological transport and interaction between them. While more physiologically relevant tissue architectures—such as naturally sprouted vasculature replicated via bioprinting—have been utilized in many other studies, they pose challenges for precise measurement[3]. These challenges include obtaining 2D imaging planes, controlling channel geometry for uniform flow, and ensuring confluent vascular layers. As a result, simpler designs, like the two-compartment model, remain prevalent. When coupled with perfusion, these platforms provide a controllable system for studying various tissue microenvironments. Among the various organ tissues fabricated using MPS techniques, the bone marrow (BM) microenvironment has recently emerged as a key focus in the MPS community[4]. The BM is crucial for regulating hematopoiesis and osteogenesis, and replicating it in vitro offers insights into blood cell development, immune responses, and bone tissue homeostasis. These advancements may also aid in studying diseases such as leukemia, anemia, and bone-related disorders.

The physical microenvironment within the BM is essential for regulating bone cell behavior, with factors such as mechanical stress, fluid flow, and pressure playing significant roles in promoting cell differentiation, maturation, and overall function[4]. In vivo, bone cells are exposed to cyclic mechanical loading and shear stress due to blood flow and bone movement, both of which influence osteogenesis and hematopoiesis. These mechanical forces help maintain bone tissue homeostasis and drive key signaling pathways involved in bone formation and remodeling. The bone microenvironment presents a more complex mechanical loading scenario than is typically seen in vascular systems. Unlike the shear stress-induced forces that predominantly affect endothelium in capillary vessels, bone cells, such as osteocytes, experience a combination of hydrostatic pressure, interstitial fluid flow,

[1]Biochemistry and Biotechnology Group, Bioscience Division, Los Alamos National Laboratory, Los Alamos, NM 87545, USA. [2]Engineered Materials Group, Material Science and Technology Division, Los Alamos National Laboratory, Los Alamos, NM, USA. [3]Transition to Operations/Readiness, Program Project Interface Division, Los Alamos National Laboratory, Los Alamos, NM, USA. [4]Department of Neurosciences, School of Medicine, University of New Mexico, Albuquerque, NM, USA. [5]Physical Chemistry and Applied Spectroscopy Group, Chemistry Division, Los Alamos National Laboratory, Los Alamos, NM, USA. ✉email: kdavisanderson@lanl.gov

and cyclic loading[4,5]. These forces are dynamic due to bone movement, physical activity, and natural remodeling processes. Osteocytes, embedded within the bone matrix, are particularly sensitive to these mechanical cues, which are crucial for regulating bone homeostasis and cell function[6]. Similarly, adipocytes, which are critical for energy storage and metabolic regulation within the BM, also respond to mechanical stimuli such as shear stress and pressure, influencing adipogenesis and the balance between osteogenesis and adipogenesis within the BM microenvironment[7]. MPS technologies provide an excellent in vitro platform for tuning the microenvironment with such mechanical forces.

Table 1shows existing BM MPS encompassing a range of platforms, from 3D static cultures of single cell types to perfused cultures of multiple cell types grown within a fluidic housing made of various materials, each demonstrating a specific aspect of the BM microenvironment. Many of these existing BM MPS demonstrated that mechanical forces, such as compression and fluid flow-induced shear stress, influence or even drive MSC differentiation into mature bone lineages[8–11]. Gabetti et al. showed that perfusion promotes the release of the early osteogenic differentiation marker alkaline phosphatase and deposited more ECM with respect to static culture[8]. In terms of adipogenesis, Liu et al. utilized a polydimethylsiloxane (PDMS)-based MPS device with two compartments separated by a porous membrane to assess adipogenesis, and found that the perfusion-based culture conditions promoted faster growth of primary preadipocytes and stimulated greater adipogenesis compared to static culture conditions[10]. Furthermore, it was reported that adipocyte differentiation in the perfusion system was more homogeneous than in the static culture condition, where they observed dispersed islands of differentiated cells, suggesting a more controllable cellular environment maintained by the perfusion-based MPS[9].

These existing devices are made from a variety of materials, as shown in Table 1, with PDMS-based soft lithography being the most commonly used approach. However, PDMS devices face several challenges, including a labor-intensive fabrication process and limitations such as molecular absorption, where substances may diffuse into the PDMS structure and become incorporated into the material matrix[4,37–42]. In terms of throughput, while multiple PDMS devices can be fabricated in a single run, modifying channel dimensions or designs presents significant limitations, as this requires recreating a master mold. Additionally, processes like plasma bonding a coverslip and punching holes to connect tubing are prone to instability, often resulting in flow leaks. Other materials, such as polycarbonate (PC) and polymethyl methacrylate (PMMA), encounter similar issues due to the nature of the layer-stacking approach. In contrast, 3D printing offers a potential solution to many of these challenges. For example, the study by Gabetti et al. demonstrated 3D printing of a bioreactor with a bone-like meshed geometry platform for the growth and differentiation of MSCs[8]. Although these designs enable physiologically relevant architecture and interstitial flow, the cylindrical geometry of the device limits its imaging capability, preventing in situ monitoring of cell growth over time. Similar challenges are observed with other methods listed in Table 1, such as bio-printing, electrospinning, and salt-leaching-based fabrication[11,35,36].

To address these limitations, this paper presents a novel fabrication method for a 3D-printed perfusion bioreactor (3D-PBR) that supports in situ growth and differentiation of MSCs while enabling co-culture with vascular cells. Our 3D-PBR is fabricated using a biocompatible resin-based printing approach, combined with a porous polyethylene terephthalate (PET) membrane, creating distinct vascular and mesenchymal stromal (MS) compartments. This platform features a flexible, scalable design and standardized fabrication, offering improved manufacturability over other existing materials. The entire 3D-PBR system, including peripheral components such as a peristaltic pump, a 3D-printed media reservoir, and perfusion tubing, fits within a 60 in^3 volume, enabling greater throughput compared to existing devices. We assessed the biocompatibility of vascular cells and MSCs within the 3D-PBR using fluorescent imaging and cell morphology analysis in situ. The development of this device provides a framework for future 3D-printed in vitro platforms, particularly for multiple cell culture models and vascular permeability assays.

BM MPS material/ Fabrication method	Fluidic mechanism	Cell type	Tissue dimension	References
PDMS/ Soft-lithography	Static; passive flow[a]; active flow[b]	a-bone marrow cells; h-MSC; h-hematopoietic stem progenitor cells; h-bone marrow mononuclear cells; h-abnormal bone marrow cells; h-abnormal erythroblast cells; h-abnormal myeloblastic cells (AML); h-abnormal megakaryoblastic cells (CML); h-fibroblast; h-plasma cell myeloma; h-osteoblasts; h-abnormal lymphoblastic cells; h-neutrophils; human umbilical vein endothelial cells (HUVEC)	2D; 3D	12–28
Silicone;PC;PMMA;PDMS/laser cutting;milling	Passive flow	h-CML; h-AML	2D; 3D	29,30
Type I collagen;PC;PMMA;COC/injection molding; hot embossing	Passive flow	h-plasma cell myeloma; h-hematopoietic progenitor cells; h-MSC; h-monocytes; h-Stromal marrow cell	2D; 3D	31–33
Silicone/conventional photo-lithography; engineered layer	Passive flow; active flow	h-AML	3D	22,34
Fibrin Bioink/3D bioprinting	Passive flow	h-MSC; HUVEC	2D, 3D	35
Heparin-Gelatin nanofibers/Co-axial electrospinning	Passive flow	h-MSC; HUVEC	3D	36
Silicone/3D-printing	Active flow	h-MSC	3D	8
Synthetic poly 3D scaffold /salt leaching process	Active flow	Bone marrow mesenchymal stromal cells	3D	11

Table 1. Current state of BM MPS and their parameters. [a]Passive flow: A mechanism driven by gravity, utilizing fluid reservoirs positioned at varying heights. [b]Active flow: a mechanism powered by syringe or peristaltic pumps for generating controlled flow. Prefix a-, animal cells; prefix h-, human cells.

Materials and methods

Bioreactor design and fabrication

Our 3D-PBR design attempts to mimic the vascular and MS compartments of the BM, as depicted in Fig. 1a. The MS compartment of the BM contains MSCs, which upon seeding proliferate initially and then later differentiate into mature adipocytes or osteoblasts based on the chemical signaling cues delivered in the cell culture media. The MS compartment also interfaces directly with a perfused endothelium-lined vasculature. Our 3D-PBR was designed to incorporate two 3D-printed compartments connected in the middle by a 0.4 µm diameter porous PET membrane (Fig. 1b-d). The vascular compartment (Fig. 1b) features a rectangular channel with dimensions of 11.8 mm × 4.8 mm × 0.8 mm (L × W × H) where media flows through Luer-lock ports. The MS compartment (Fig. 1c) includes an oval-shaped channel (15.8 mm × 4.8 mm × 0.8 mm) with barbed ports that enables the user to inject the MSC-laden ECM on either side. Located in the middle of the two compartments is a PET membrane (Fig. 1d) that spatially separates the two compartments while still permitting media transport and cellular

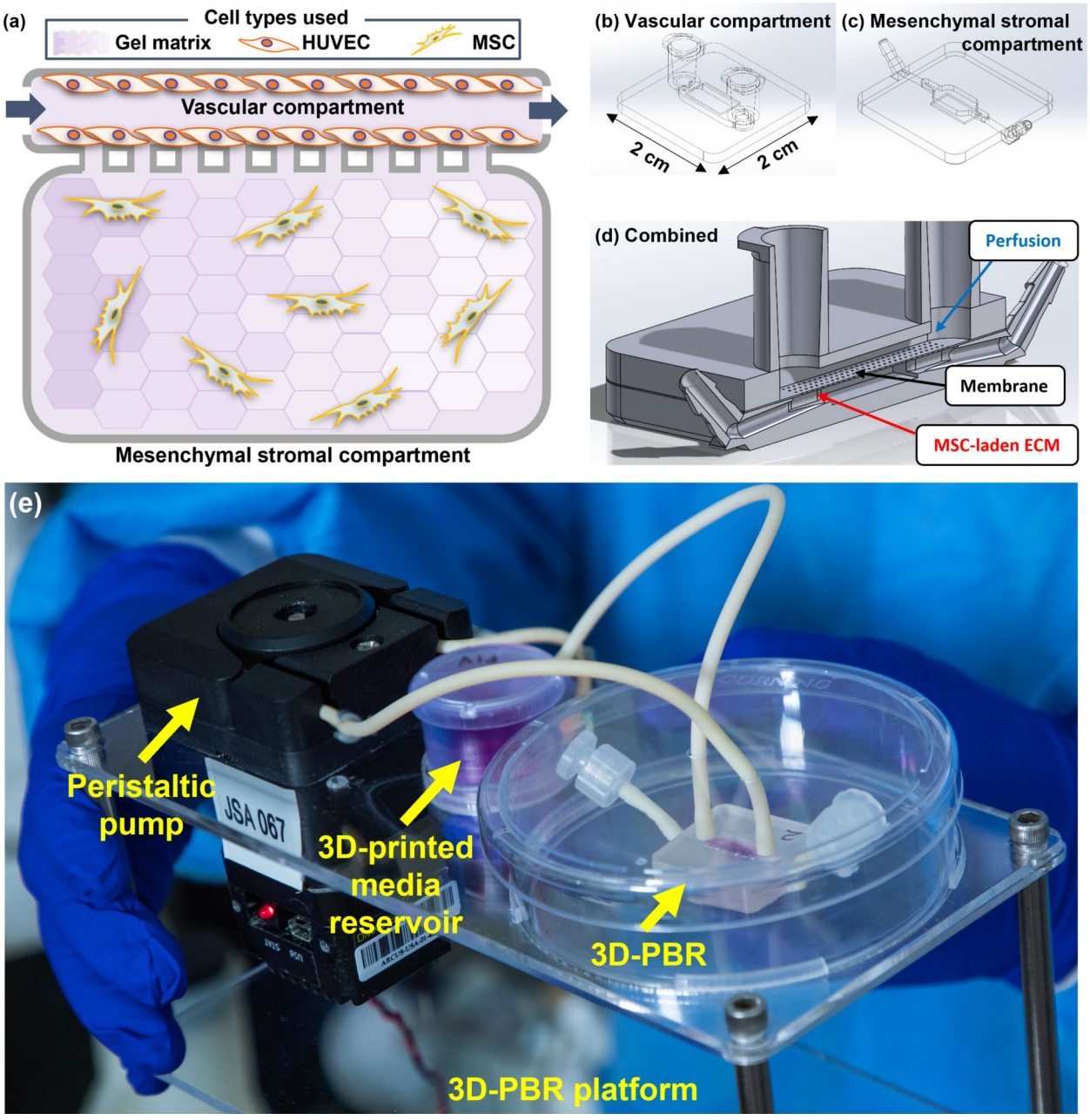

Fig. 1. Schematic of the 3D-PBR, illustrating (**a**) the biological components and cellular compartments, transparent views of (**b**) the 3D CAD view of the vascular compartment, (**c**) the 3D CAD view of the mesenchymal stromal compartment, (**d**) the 3D CAD cross-sectional view of the fully assembled 3D-PBR, and (**e**) the fully assembled 3D-PBR system with the modular peristaltic pump and 3D-printed cell culture media reservoir.

interaction. The fully assembled 3D-PBR system, includes a modular peristaltic pump, as well as a 3D-printed cell culture media reservoir, all of which are shown in Fig. 1e. These components when fully assembled are used to establish a dynamic 3D microenvironment in vitro. The intent for using two different compartments with their own unique geometries was for the purpose of having two complex microenvironments exist in unison.

Fig. 2 illustrates the steps involved in 3D-PBR fabrication. Our fabrication process enables rapid prototyping and ease of assembly once all the components needed have been printed and sterilized thoroughly. The upper and lower chamber geometries of the 3D-PBR was created using 3D drawing software (Solidworks), and the files were directly uploaded to the Low Force Stereolithography 3D-printer (Formlabs 3B). The vascular and MS compartments were 3D-printed using a biocompatible surgical guide resin, which is a composite of a methacrylate monomer (25 – 45% by weight) and urethane dimethacrylate (55 – 75% by weight) which is hardened via a photoinitator (1 – 2% by weight), heat, and UV light (Formlabs).

After the printing process is completed, the devices were removed from the printing platform and washed three times in a 99.7% isopropyl alcohol solution (Sigma Aldrich). The first wash was a general wash, the second aimed at clearing excess resin from ports and channels, and the third involved a magnetically coupled impeller to agitate the isopropyl alcohol for a final wash. Bathing each of the newly printed components in isopropyl alcohol before curing is critical to ensure that none of the channels were clogged due to excess resin and to achieve a tight seal between the interior surfaces of each device.

After the washing steps were completed, each of the 3D-PBR pieces received a thin layer of resin coating on the interior compartments and exterior insets, then immediately cured with UV light (Dy Max Bluewave 200). The purpose of layering a light coat of resin on specific parts of the 3D-printed pieces was to enhance the optical clarity of the device halves for allowing high-quality imaging. Subsequently, the 3D-printed parts were fully cured at 60 °C and 405 nm wavelength UV light for 30 min (FormCure).

A silicone-based adhesive (3 M; 91022) was precisely cut according to the outline (Solid Edge) of each compartment using a CO2 laser cutter (Universal Laser Systems). The adhesive layers were then applied to the interior surfaces of the 3D-PBR compartments. To ensure sterility, the components were autoclaved together at 121 °C and 15 psi for 30 min (Tuttnauer). The assembly of the two 3D-PBR compartments with a porous membrane using the adhesive layer is shown in Fig. 3 (note that the transparent adhesive layers and porous membrane were not included in these example images). A mold-like plate (Fig. 3a) was 3D-printed to position the vascular compartment upside down (Fig. 3b-c), with a porous PET membrane (Corning; 3450) added during this step. In Fig. 3d, the MS compartment was placed on top of the vascular compartment, with four metal posts attached to an acrylic plate that helps with the consistent alignment of four corners of each compartment (image not shown). Subsequently, a roller was used to apply pressure to activate the adhesive layers (Fig. 3e). All assembly steps of the 3D-PBR were performed in a biosafety cabinet using aseptic techniques. Finally, the fully assembled 3D-PBR (Fig. 3f) was injected with 1 mL of 1 × Phosphate Buffered Saline (PBS) (Gibco) into each compartment and port to check for leaks. The excess PBS was then removed via vacuum aspiration, and the 3D-PBRs were kept in a sterile environment until ready for cell culture.

Micro-CT scan of the 3D-PBR

To measure the internal dimensions of the constructed 3D-PBR, a μCT scan was performed using an Xradia 520 Versa (Carl Zeiss X-ray Microscopy). The first scan covered the entire 3D-PBR at a voxel size of 16.5 μm, and a second region-of-interest scan was conducted at a higher resolution of 1.1 μm voxel size, specifically

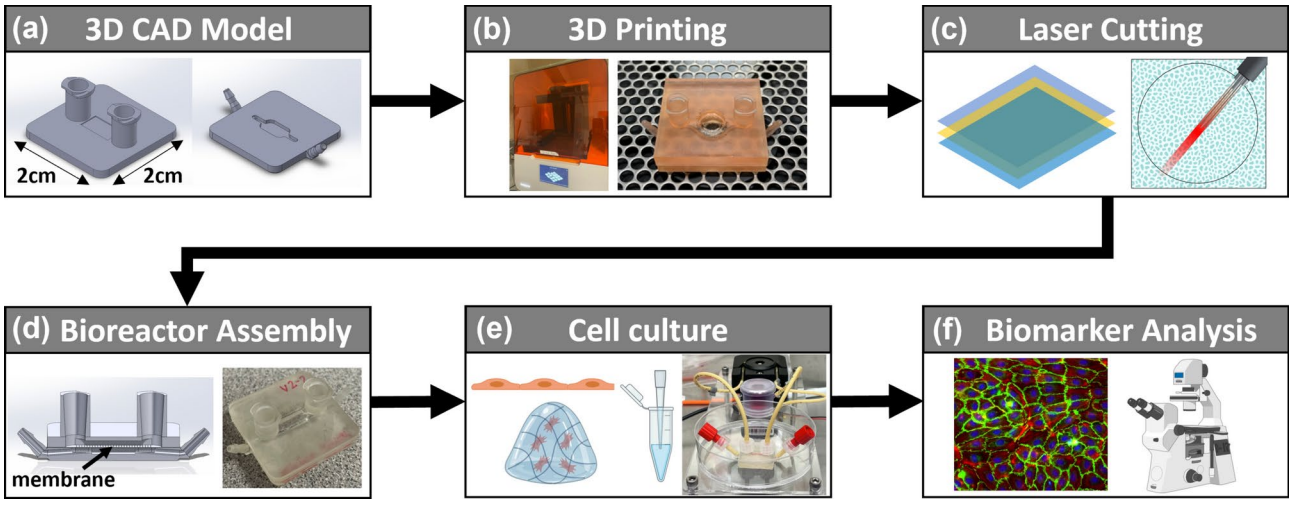

Fig. 2. 3D-PBR fabrication and workflow steps, including (**a**) generating a 3D CAD model depicting the vascular and mesenchymal stromal compartments, (**b**) 3D printing and curing processes, (**c**) laser cutting of adhesives and porous membrane, (**d**) assembly of the 3D-PBR with two compartments connected by a porous membrane, (**e**) complete assembly with a 3D-printed media reservoir and a peristaltic pump, followed by injection of cells and matrices, and (**f**) fixation of samples for image analysis.

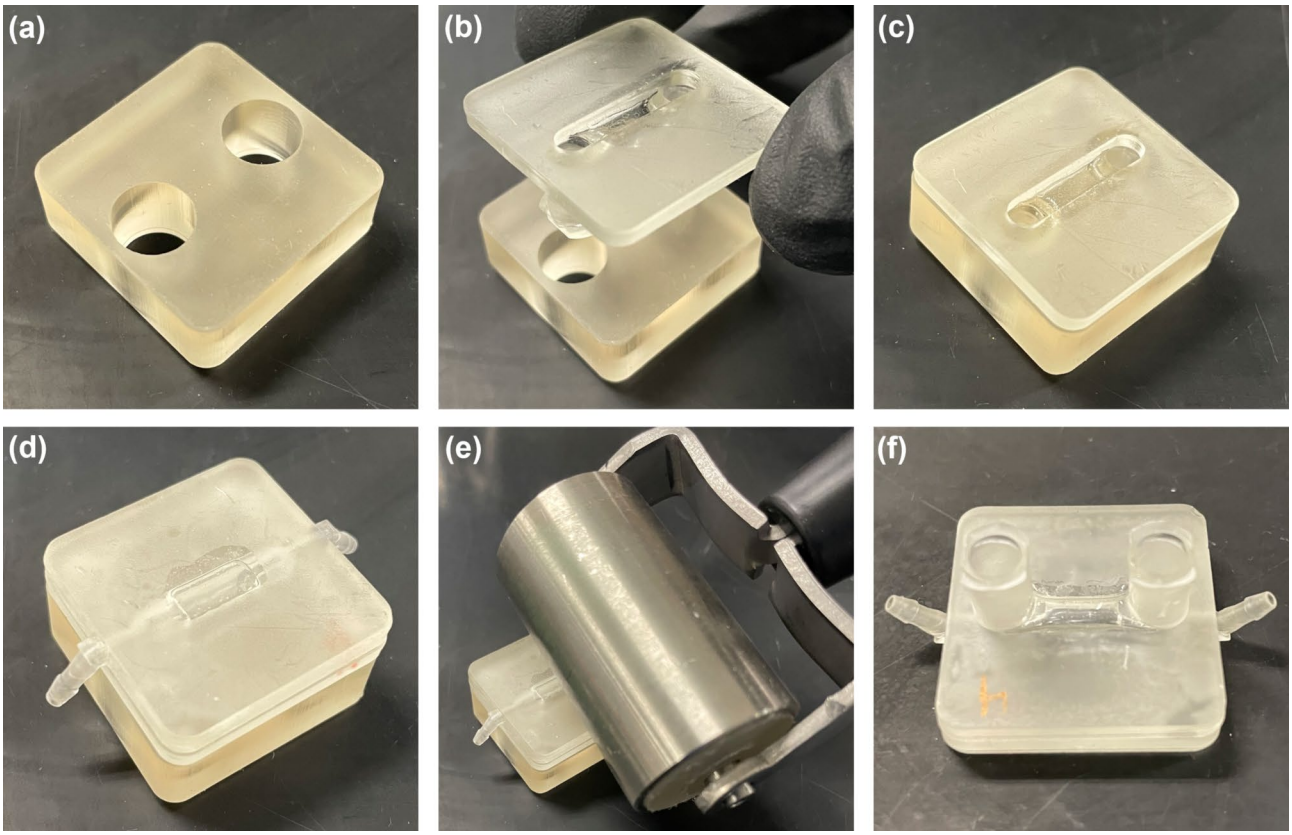

Fig. 3. Assembly process of the vascular and MS compartments in the 3D-PBR.

showcasing the interface between the vascular and MS compartments (Fig. 4). Both images were collected at 80 kVp, 7W power, 5001 radiographs, and 1.5 s exposure per radiograph. The 3D data were rendered and measured in Avizo for Industrial Inspection (Thermo Fisher Scientific). The yellow regions in the scan represent internal void spaces within the 3D-PBR, demonstrating the tight seal between the two compartments and preventing potential leakage during cell culture under media perfusion. The measured internal dimensions were used to estimate the shear stress level experienced by HUVECs in the vascular compartment.

Peristaltic pump operation and flow measurements

The peristaltic pump consisted of a 4-roller pump head (Langer Instruments) controlled by a stepper motor (Arcus Technologies). A biocompatible tubing (1.3 mm ID, Cole-Palmer) was used to connect the 3D-PBR to the pump and the 3D-printed reservoir (Fig. 1e). The pump rotational speed, torque, and duration were controlled by a custom script programmed in LabVIEW to cyclically modulate flow within the 3D-PBR.

Figure 5represents the mean flow rate within 3D-PBR setup with respect to the input pump speed measured by the Microfluidic Thermal Flow Sensor (Darwin Microfluidics). Each condition was performed in triplicate, and each of the averaged quantities consisted of 800 individual flow rates acquired over 40 s. The 3D-PBR was operated at two different flow rates, including 23 µL/min and 100 µL/min. These values were chosen based on previous studies, which reported that the 100 µL/min flow rate has been demonstrated to be effective in a bone-generating hydrogel BR, and lower perfusion rates are often utilized to account for smaller tissue mass[15,43].

The wall shear stress at the membrane surface was estimated based on the solution to Poiseuille flow for an incompressible Newtonian fluid (described by the Navier–Stokes equations) in a rectangular channel.

$$\text{Wall Shear Stress} = \frac{6\text{Q} \cdot \mu}{\text{h}^2 \cdot w} \tag{1}$$

where Q, µ, h, and w represent the volumetric flow rate, dynamic viscosity of the fluid, and the height and width of the channel cross-section, respectively. The shear stress experienced by HUVECs within the 3D-PBR was calculated to be 6×10^{-3} dyn/cm^2 and 2.5×10^{-2} dyn/cm^2 for flow rates of 23 µL/min and 100 µL/min, respectfully.

Cell culture

2D cell expansion

All cells and cell reagents were purchased from Lonza and were used in accordance with the manufacturer's recommendations. Human BM-derived MSCs were expanded on 2D tissue culture-treated plates and maintained in MSCGM™ Mesenchymal Stem Cell Growth Medium BulletKit™ (Lonza). Additionally, single-donor human

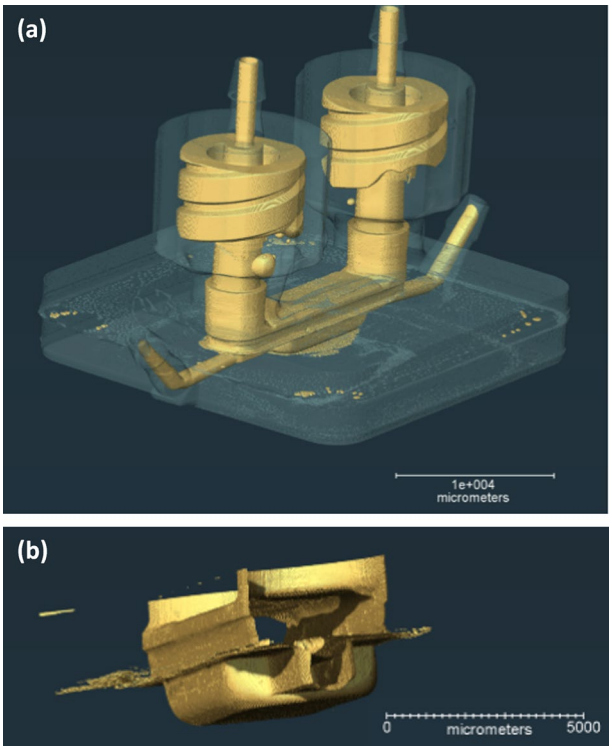

Fig. 4. µCT scan of the 3D-PBR, illustrating (**a**) a full scan at a 16.5 µm voxel size and (**b**) a region-of-interest scan at a 1.1 µm voxel size, showcasing the interface between the vascular and mesenchymal stromal compartments.

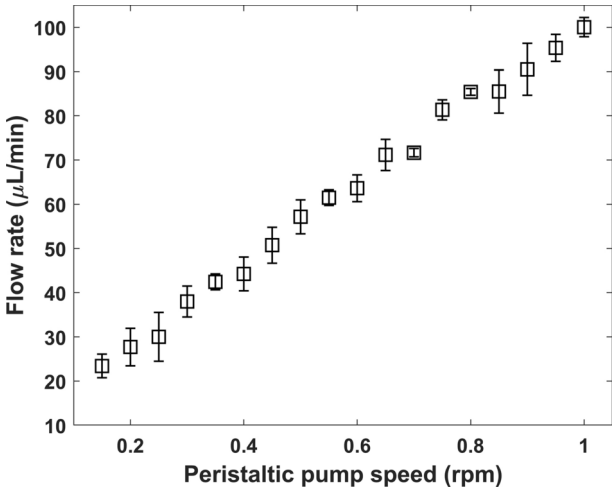

Fig. 5. Mean flow rate from the 3D-PBR setup across pump speeds.

umbilical vein endothelial cells (HUVECs) without VEGF were separately cultured on 2D tissue culture-treated plates and maintained in EGM-2 medium (Lonza). All cells were incubated at 5% CO_2 and 37 °C in a humidified incubator (Thermo Fischer Scientific), with the culture media being changed every 2 – 4 days. Once the cells reached approximately 80% confluency, they were detached using Trypsin/EDTA (Lonza) and Trypsin Neutralizing Solution (Lonza) before being plated and passaged to static well plates or 3D-PBRs (passage 3).

3D cell growth and differentiation

Surface modifications were performed on the static well plates and 3D-PBRs prior to cell seeding. A 50 µg/mL solution of type I collagen (Sigma-Aldrich; C2249) was added, and the static well plates and 3D-PBRs were incubated overnight at 4 °C. After incubation, the collagen was removed, and the platforms were washed with PBS. MSCs were suspended in the collagen-fibrin gel with a final concentration of 3.8×10^4 for osteogenic

differentiation and 2.6×10^5cells/mL for adipogenic differentiation, which were conducted separately. The gel solution was crosslinked by mixing the two neutralized components at a ratio of 1:3[15]. The first component contained 0.24 mL of sterile MSCGM, 0.25 mL of 40 mg/mL fibrinogen (Millipore; 341,578-500 mg), and 0.01 mL of 5 mg/mL aprotinin (Sigma-Aldrich; A3428) kept at 37 °C. The second component contained 0.317 mL of MSCGM with MSCs, 0.133 mL of 3 mg/mL collagen I (Sigma-Aldrich; C2249), and 0.05 mL of 20 U/mL thrombin (Millipore; 605,195) kept at 4 °C. The mixture of the two components at a ratio of 1:3 (0.1 mL) was carefully pipetted into static well plates or the MS compartment of the 3D-PBR and allowed to gel for 20 min at 37 °C in the incubator. MSCs were separately differentiated into adipocytes or osteoblasts with Human Mesenchymal Stem Cell (hMSC) Adipogenic Differentiation Medium BulletKit™ and hMSC Osteogenic Differentiation Medium BulletKit™ from Lonza, respectively. In the 3D-PBR, a 1×10^6 cells/mL HUVECs were added to the vascular compartment to create a confluent monolayer on day 21 of differentiation of either osteoblasts or adipocytes. The HUVECs were maintained for 4 days in EGM-2. Each 3D-PBR culture condition was performed in triplicate, with HUVECs/osteocytes and HUVECs/adipocytes.

Immunohistochemical staining

For immunohistochemical (IHC) staining, cells were fixed with 4% paraformaldehyde, permeabilized with 0.1% Triton X-100, and blocked using 3% BSA in DPBS. Each step required injection and washing of reagents through the vascular compartment, followed by overnight incubation at 4 °C to ensure thorough exposure of the cells within the 3D-PBRs.

For staining HUVECs, a VE-Cadherin mouse monoclonal antibody (Invitrogen; MA1-198) was used at a concentration of 3 µg/mL in blocking buffer for 1 h at room temperature. Subsequently, the cells were incubated with Goat anti-Mouse IgG (H + L) Superclonal™ Secondary Antibody, Alexa Fluor® 488 conjugate (Invitrogen; A28175) at a dilution of 1:500 for 1 h at room temperature in the dark. A mixture of ActinRed™ 555 ReadyProbes™ Reagent (Rhodamine Phalloidin, Invitrogen; R37112) and NucBlue™ Fixed Cell ReadyProbes™ Reagent (DAPI, Invitrogen; R37606) in blocking buffer was then injected into the vascular compartment and incubated overnight at 4 °C.

For 3D-PBRs containing HUVECs and adipocytes, HCS LipidTOX™ Green Neutral Lipid Stain (Invitrogen; H34475) was used instead of VE-Cadherin to prevent signal overlap, while the same steps were applied for DAPI and Rhodamine Phalloidin staining.

Fluorescent imaging

Images were recorded on a wide-field fluorescence inverted microscope (ZEISS; Axio Observer.Z1) with a 1388×1040 pixels CCD camera (ZEISS; AxioCam MRm) at 4x, 10x, and 20x magnification. A mercury lamp was used for fluorescence illumination, with a fluorescence filter cube for imaging DAPI, Alexa Fluor 488, and Alexa Fluor 555 labeled cells. Image acquisition was controlled through ZEN software (ZEISS).

Cell viability measurement

Cell viability was assessed using Acridine Orange/Propidium Iodide (AO/PI) staining (Nexcelcom Bioscience; CS2-0106-5ML). The 3D-PBRs were cultured with either HUVECs or MSCs, but no coculture was conducted for the viability assay, as the initial 4 days of culture required feeding of different media for each cell type through the vascular compartment.

Each day, 3D-PBRs were detached from perfusion and filled with a 1:1 mixture (0.2 mL) of AO/PI and culture medium through the vascular compartment. They were then incubated for 1 h at 37 °C and 5% CO_2 until the samples were imaged with a fluorescent microscope. It should be noted that the reagent is formulated not to produce a double positive signal; therefore, live and dead signals were recorded separately in different fluorescent channels.

Visible cells were detected and counted automatically using a multi-feature-based cell tracking algorithm previously developed by the author[44,45], while those that were out-of-focus or partially visible due to proximity to image boundaries were excluded. After image acquisition, the AO/PI-stained samples were discarded and not reused.

Cell morphological analysis

To compare the differentiation rate of MSCs between the 3D static well plate and 3D-PBR, we analyzed the IHC images using a multi-feature-based cell tracking algorithm[44,45]. Osteogenic differentiation was evaluated using three common shape descriptors for cell morphology characterization[46,47].

$$\text{Roundness} = \frac{4\pi \cdot \text{area}}{(\text{convex perimeter})^2} \tag{2}$$

$$\text{Eccentricity} = \sqrt{1 - \frac{\text{minor axis length}^2}{\text{major axis length}^2}} \tag{3}$$

$$\text{Solidity} = \frac{\text{Area}}{\text{Convex Area}} \tag{4}$$

Adipogenic differentiation was assessed by measuring the diameter and normalized raw intensity of lipid droplets, as well as the percentage of differentiated adipocytes among the total cell count, indicating adipocyte maturation.

Statistical analysis

Statistical analyses were performed using JMP software (SAS, Cary, NC, USA). The Shapiro–Wilk test was used to assess the normality of the data distribution. Since not all groups showed a normal distribution ($p < 0.05$), a Wilcoxon rank-sum test (also known as the Mann–Whitney U test) was used to assess differences between the Static and 3D-PBR cultured MSCs. The Wilcoxon test was chosen as a non-parametric alternative to the t-test for comparing two independent samples when normality could not be assumed for one group.

For Fig. 7, each culture condition was conducted in triplicate, with each averaged quantity consisting of more than 80 individually identified cells. For Fig. 8, each culture condition was also conducted in triplicate, with each averaged quantity comprising more than 200 individually identified cells and more than 500 lipid droplets. The difference in the range of cell numbers between Fig. 7 and Fig. 8 was due to differing differentiation protocols for MSCs, where adipogenesis required a much higher seeding density than osteogenesis.

For all statistical analyses, significance was set at $p < 0.05$. Each box plot displays the mean, median, lower and upper quartiles, outliers (identified using the interquartile range), and the minimum and maximum values, excluding outliers. Results are reported with p-values denoted by asterisks (*) as follows: * significant at $p < 0.05$, ** significant at $p < 0.01$, *** significant at $p < 0.001$, and **** significant at $p < 0.0001$. The exact p-values are provided in the results section. A p-value of < 0.05 was considered the threshold for statistical significance.

Results

Cell viability

The viability of MSCs and HUVECs grown in the 3D-PBR was measured via AOPI staining. Figure 6a-b show the representative fluorescent images of these cells with overlayed channels, where the green fluorescence marks healthy cells, and the red fluorescence marks apoptotic cells. HUVECs were seeded at a concentration of 1×10^6 cells/mL to ensure the formation of a confluent 2D monolayer on the permeable membrane within 1 day. The MSC-laden gel had a concentration of 2.6×10^5 cells/mL when injected into the 3D MS compartment.

While the green fluorescence clearly marks the nuclei, most of the apoptotic cells marked by the red fluorescence appear to be nuclear fragments rather than whole cells. Therefore, the percent viability shown in Fig. 6c represents a lower bound of the true cell viability, as individual fragments were counted as apoptotic cells. The daily viability measurements were conducted in triplicate, with each averaged quantity consisting of more than 800 individually identified cells. No significant variation was found in the percent viability across different days, which was less than 2% for both HUVECs and MSCs. The mean percent cell viability in the 3D-PBR across all time points was 92% and 91% for the MSCs and HUVECs, respectively.

It should be noted that we measured AOPI-based cell viability separately for HUVECs and MSCs over four consecutive days to demonstrate the biocompatibility of 3D-PBR. The viability of cocultured samples, which

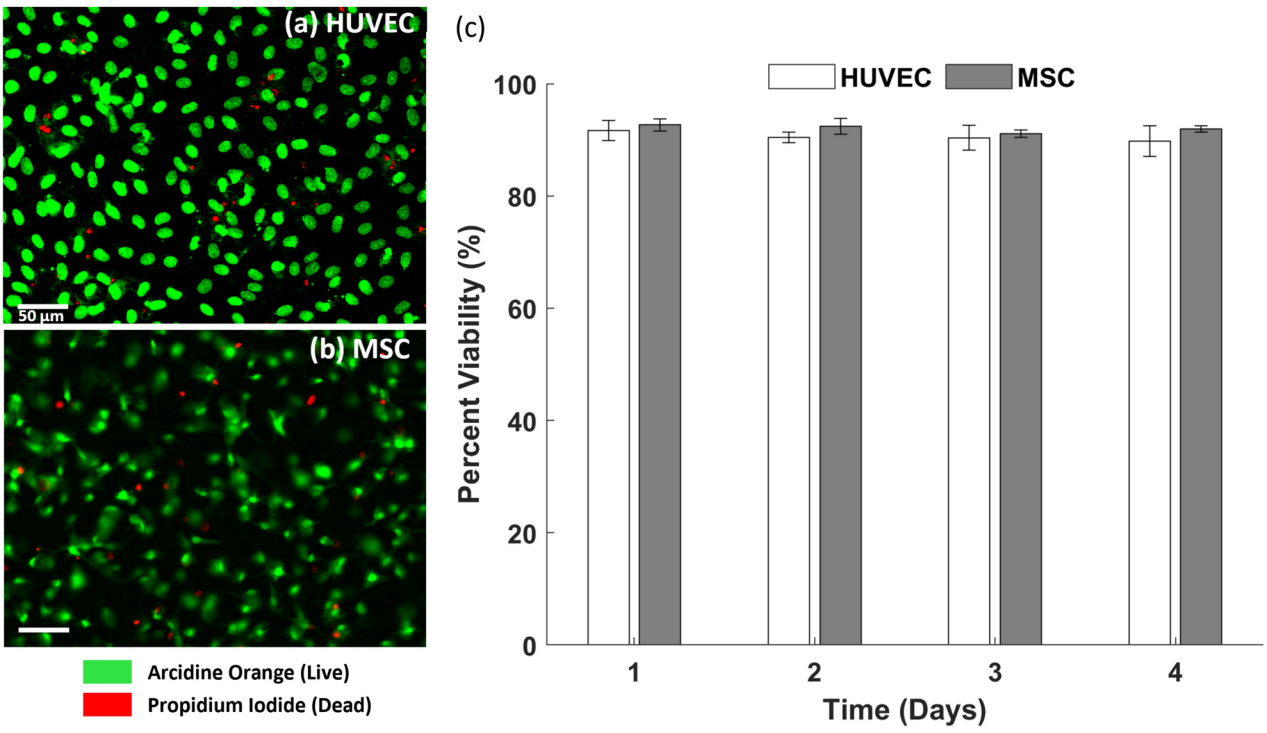

Fig. 6. Cell viability in the 3D-PBR was assessed using AOPI staining. Representative fluorescent images of (**a**) HUVEC and (**b**) MSC are shown. (**c**) The percentage of cell viability over 4 days is presented. The scale bar indicates 50 µm.

underwent a full 25 days of culture, was assessed solely via IHC images at their terminal time points. This approach was adopted to prevent potential toxic effects resulting from prolonged AOPI exposure.

Immunohistochemical analysis

Fig. 7a represents three stages of osteogenic differentiation of MSCs in human BM tissue. MSCs serve as the primary progenitor cells for osteoblasts, which typically line the bone surfaces and exhibit a cobblestone morphology. Osteocytes, mature bone cells, are then derived from osteoblasts, becoming embedded within the mineralized bone matrix[48,49]. MSCs in both static 3D culture and 3D-PBR environments were exposed to osteogenic differentiation media for 21 days while suspended in the gel matrix (creating a 3D microenvironment). Each culture condition was conducted in triplicate, with each averaged quantity consisting of more than 80 individually identified cells. In the static 3D environment, the MSCs primarily showed spindle-shaped morphologies (resembling undifferentiated MSCs, Figure 7a-c). In contrast, the MSCs cultured in the 3D-PBRs exhibited a higher degree of osteogenic maturity, evident from their roundness and length of dendritic extensions (Fig. 7c). These differences are further highlighted in the cell morphology analysis (Figure 7d-f). Roundness and eccentricity most strongly indicate the morphological differences between the MSCs differentiated under static 3D culture plates versus 3D-PBR ($p < 0.0001$). The mean solidity was 8% lower in the 3D-PBR case, primarily due to the more irregular boundaries with dendritic extensions ($p = 0.0034$).

It should be noted that the commercial MSC-osteoblast differentiation media used in our study was originally designed for 2D static culture, so the further differentiation of osteoblasts into osteocytes within a dynamic

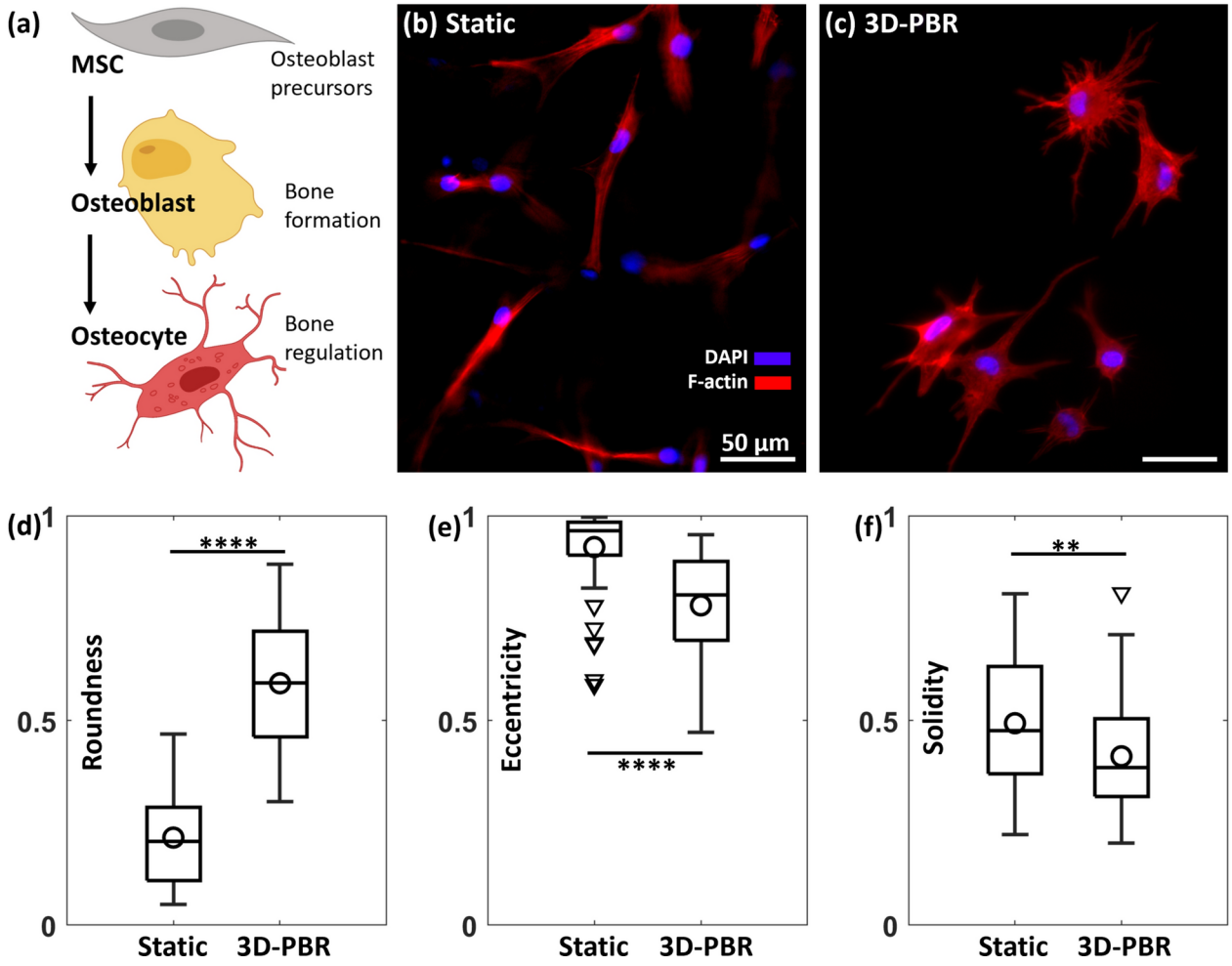

Fig. 7. (**a**) Illustration depicting the three stages of osteogenesis. Representative IHC images showing nuclei (DAPI) and cytoskeleton (F-actin) staining of MSCs cultured (**b**) statically within a 3D standard culture plate, and (**c**) dynamically within the 3D-PBR for 21 days using osteogenic differentiation media. Scale bar: 50 µm. Image-based cell morphology analysis comparing (**d**) roundness, (**e**) eccentricity, and (**f**) solidity of MSCs cultured under static conditions versus 3D-PBR. Each box plot displays the mean, median, lower and upper quartiles, outliers (identified using the interquartile range), as well as the minimum and maximum values excluding outliers. p-values are denoted with asterisks (*) as follows: ** significant at $p < 0.01$ and **** significant at $p < 0.0001$.

3D tissue environment is not surprising. While the precise mechanisms controlling the differentiation of osteoblasts into osteocytes embedded in the bone matrix remain elusive, previous research has shown that fluid flow-induced shear stress significantly increases the expression of osteogenic genes in MSCs[6,7,43]. The distinct morphology of osteocytes was not observed in the 3D static culture samples. The absence of flow and pressure in the static 3D culture environment may be a potential reason for their slower differentiation compared to the more physiologically relevant bone matrix environment provided by the 3D-PBR.

The adipogenesis of MSCs was assessed in both the 3D-PBR and static 3D culture plate. MSCs in both environments were exposed to adipogenic differentiation media for 21 days while suspended in a gel matrix. Each culture condition was conducted in triplicate, with each averaged quantity comprising individually identified cells (>200) and lipid droplets (>500). Figure 8a-f displays the IHC staining using three different markers, visualizing F-actin, lipid droplets, and the nucleus of the adipocytes. In both the static 3D culture and 3D-PBR samples, varying degrees of adipocyte maturation were observed, particularly with regard to lipid size and density. Figure 8g compares the percentage of differentiated adipocytes exhibiting visible intracellular lipid droplet formation out of the total number of cells. However, no significant differences were observed between the two culture conditions ($p = 0.9294$). Figure 8h-i compares the estimated diameter and normalized mean fluorescent intensity of all segmented individual lipid droplets. The mean diameter of the lipid droplets between the two conditions was similar, while the 3D-PBR included more lipid droplets with a diameter greater than

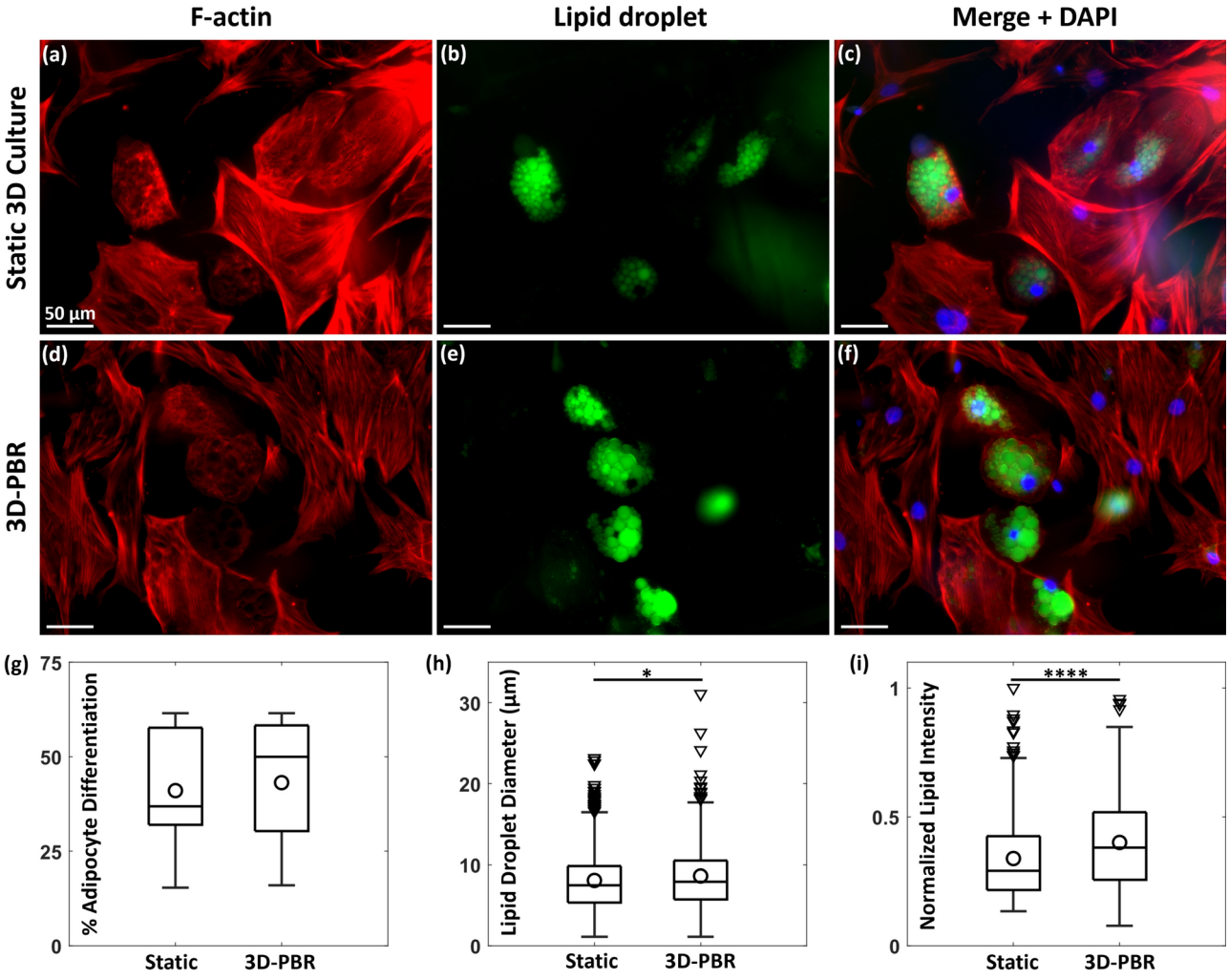

Fig. 8. Representative IHC images showing nuclei (DAPI), neutral lipid droplet (LipidTOX™ Green), and cytoskeleton (F-actin) staining of MSCs cultured (**a**)-(**c**) statically within a 3D standard culture plate, and (**d**)-(**f**) dynamically within the 3D-PBR (23 µL/min) for 21 days using adipogenic differentiation media. The scale bar indicates 50 µm. Image-based cell morphology analysis comparing (**g**) percent differentiated adipocyte, (**h**) lipid droplet diameter, and (**i**) normalized lipid intensity of MSCs cultured under static conditions vs. 3D-PBR. Each box chart displays the mean, median, lower and upper quartiles, outliers (identified using the interquartile range), as well as the minimum and maximum values excluding outliers. *p*-values are denoted with asterisks (*) as follows: * significant at $p < 0.05$ and **** significant at $p < 0.0001$.

20 µm ($p = 0.0239$). Consequently, the presence of these larger diameter lipid droplets resulted in a higher mean fluorescent intensity of these lipid droplets in the 3D-PBR than in the static culture condition, indicating possible differences in maturation stages ($p < 0.0001$).

While few recent studies have reported accelerated differentiation of adipocytes under perfusion conditions within PDMS devices[10,50], it is well investigated that high cell density (post-confluency) can enhance adipogenic differentiation of MSCs, suggesting the secretion of signaling factors or cell-contact-mediated signaling[9]. According to the manufacturer's protocol, reaching post-confluency of MSCs was a required step before applying the adipogenic differentiation media. As a result, the percentage of differentiated adipocytes may be more influenced by paracrine signaling rather than physical factors such as flow, pressure, or the 3D architecture of the tissue environment, which did influence lipid droplet maturation in terms of their diameter and fluorescent intensity.

Overall, our observations demonstrate that both the 3D-PBR and static 3D culture methods can support adipogenic differentiation of MSCs. However, the specific contributions of physical and chemical factors in each environment warrant further investigation for a comprehensive understanding of adipogenesis within the 3D-PBR system. Table 2 below presents the numerical values for the mean and standard deviation of the cell morphological parameters shown in Fig. 7 and Fig. 8.

Following the differentiation process (post 21 days) of osteocytes or adipocytes, HUVECs were seeded and cultured for an additional 4 days with endothelial growth media under two different flow rates (each condition was conducted in triplicate). These cases are compared to the static 2D culture of HUVECs in Fig. 9. Notably, HUVECs grown in static 2D culture did not form adherens junctions as pronounced as those in the 3D-PBR. In Fig. 9a-c, the confluent state of HUVECs under static culture exhibits visible gaps between cells that did not significantly reduce after 4 days of culture.

Figure 9d-f illustrates HUVECs cultured under a lower flow rate of 23 µL/min, where the cell morphology significantly differs from the static cultures. Stretched actin filaments are visible (Fig. 9d), along with adherens junctions between cells via VE-cadherin signals (Fig. 9e). Similarly, HUVECs cultured under a higher flow rate of 100 µL/min (Fig. 9g-i) display similar features as the lower flow rate cases, including an elongated appearance of actin filaments and strong signals of adherens junctions. Notably, the addition of HUVECs to the 3D-PBR did not seem to significantly change the morphologies of the osteocytes or adipocytes over the 4-day period. This was expected, as the MSCs were already differentiated over 21 days under differentiation media, and only the endothelial growth media was perfused during the last 4 days to maintain the confluent HUVEC monolayer.

Discussion

In this study, we successfully fabricated and sustained a dynamic 3D tissue microenvironment using 3D-printing technologies to facilitate the in situ growth and differentiation of human BM-derived MSCs. While PDMS-based microfluidic devices are widely utilized, their well-known drawbacks, such as high molecular absorption, limited durability, low reproducibility, and customization challenges, pose limitations[4,37]. The layered molding technique inherent to PDMS devices also imposes constraints on device complexity. Additionally, PDMS exhibits unfavorable properties for BM research, including its tendency to absorb culture medium components and interact with drugs. For example, Van Meer et al. reported a concentration reduction of over 50% with verapamil after a three-hour incubation using liquid chromatography, while Wang et al. observed molecular absorption into PDMS microfluidic channels, resulting in concentration reductions of 8% at 0.5 h and 22% at 4.5 h, all at 25 °C. This absorption can compromise the accuracy of molecular analyses conducted using such microfluidic devices. The hydrophobicity of PDMS has been associated with its drug absorbent properties[42]; however, it is important to note that hydrophobicity alone does not fully explain this characteristic[41]. Nonetheless, the reduced hydrophobicity of methacrylate polymers[38,40], as utilized in our 3D-PBR, compared to PDMS[39], may lead to a decrease in drug absorbance[4]. Although, the drug absorbance properties of methacrylate polymers remain to be examined.

The integration of 3D printing into microfluidic development has faced challenges, primarily linked to the unverified biocompatibility of resins[4,37]. In contrast, our 3D-PBR was fabricated using readily available industry-standard materials and supplies, including resin, adhesives, PET membrane, human cell lines, and media, without any custom modifications. Additionally, the 3D printing approach allowed us to create an integrated luer-lock system, enabling quick fluidic connections without the risk of dislodging barbs from the device. This approach supports the widespread adoption of 3D-printed devices and promotes the standardization of MPS among bioscience researchers.

As shown in Table 1, many existing devices focus on modeling specific aspects or functions of BM, often targeting mechanical stressors, ECM, or cellular crosstalk. While these systems are effective for studying individual BM components, they are limited by challenges in manufacturing, scalability, flexibility in design, and in situ monitoring. In contrast, our 3D-PBR offers a more comprehensive approach by integrating co-culture and mechanical flow within a compartmentalized three-dimensional environment that can be monitored in situ. Unlike single-purpose devices, our 3D-PBR is versatile and easily modifiable, enabling the simulation

Mean ± standard deviation	Roundness	Eccentricity	Solidity	% Adipocyte differentiation	Lipid diameter (µm)	Normalized lipid intensity
Static	0.21 ± 0.11	0.92 ± 0.10	0.49 ± 0.15	41.02 ± 15.85	8.05 ± 3.94	0.34 ± 0.16
3D-PBR	0.59 ± 0.16	0.78 ± 0.13	0.41 ± 0.13	43.13 ± 17.04	8.60 ± 4.16	0.40 ± 0.18

Table 2. Mean ± standard deviation of cell morphological parameters.

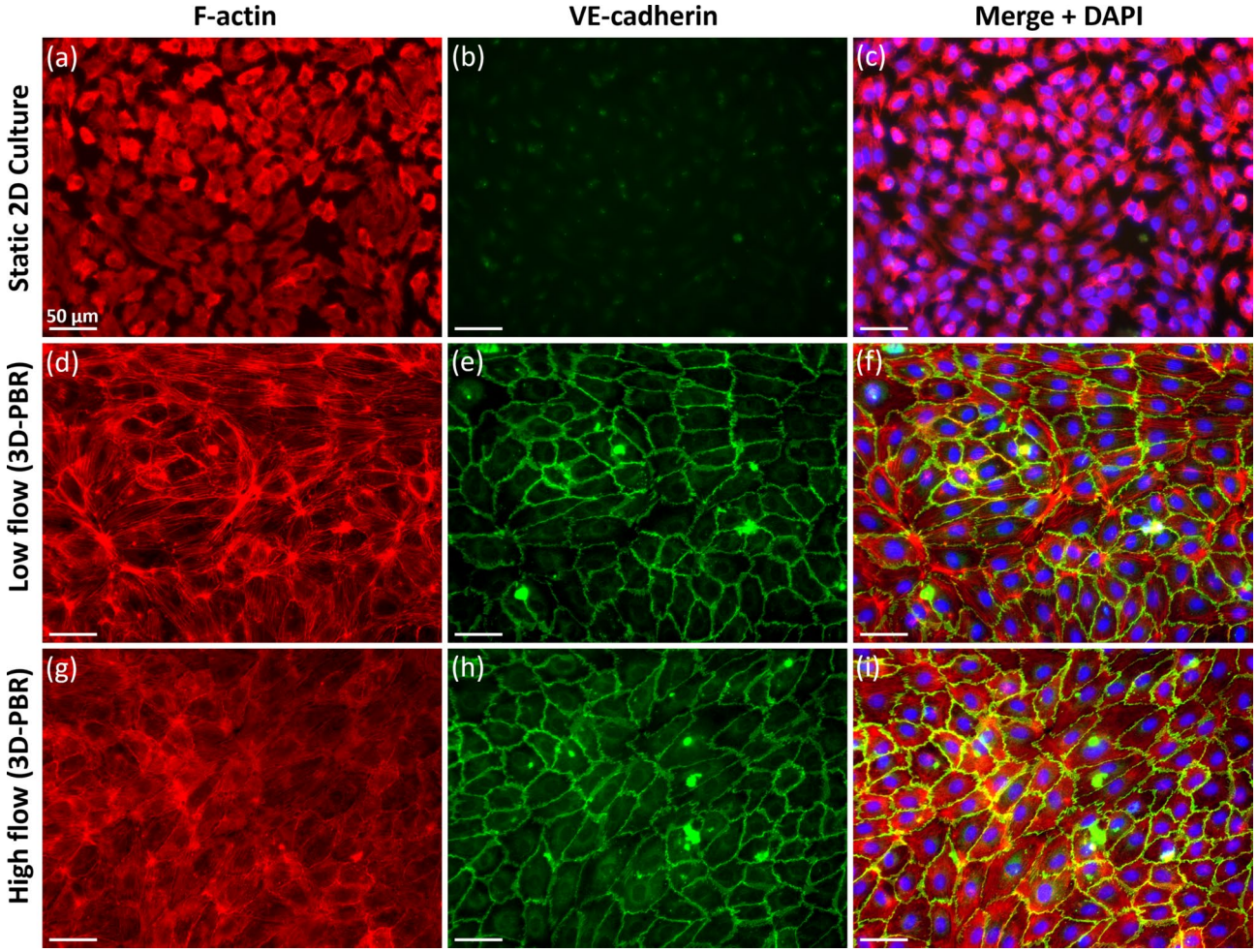

Fig. 9. Representative IHC images showing nuclei (DAPI), adherens junctions (VE-cadherin), and cytoskeleton (F-actin) staining of HUVECs cultured (**a**)–(**c**) statically within a 2D standard culture plate, dynamically within the 3D-PBR under flow rate at (**d**)–(**f**) 23 µL/min, and (**g**)–(**i**) 100 µL/min for 4 days. The scale bar indicates 50 µm.

of various tissue microenvironments tailored to specific experimental needs. While 3D printing is becoming more common in bioengineering, the novelty of our system lies in its flexibility, which supports a wide range of research applications, including studies on cellular differentiation, vascularization, and the mechanobiological effects of flow across various tissue microenvironments.

In summary, our study has provided valuable insights into the performance of the 3D-PBR in recapitulating complex tissue models. We demonstrated the feasibility of culturing MSCs and inducing osteogenesis and adipogenesis within the 3D-PBR, shedding light on the potential applications of this system in better understanding the MSCs lineage commitment. Variations in cell morphology were observed during the osteogenic differentiation of MSCs (Fig. 7), while an enhanced maturation stage of the lipid droplets was noted during MSCs' adipogenic differentiation (Fig. 8). This suggests that the dynamic 3D tissue microenvironment provided by the 3D-PBR may promote a more physiologically relevant differentiation process for MSCs. Additionally, the integration of mature vessels by HUVECs in the 3D-PBR further showcases its versatility for coculture studies (Fig. 9). The success of our 3D-PBR in accurately replicating physiologically relevant osteocyte, adipocyte, and endothelium-lined vasculature within a single device opens up exciting possibilities for future research in bone mechanobiology.

There are several limitations in the present study. First, although our 3D-PBR design enables the coculture of multiple cell types, we did not quantify the effect of angiocrine factors produced by vascular cells on the growth and differentiation of MSCs through detailed gene expression analysis, as our study primarily focused on assessing the biocompatibility of the device via in situ analysis. Second, vascular cells were introduced after MSCs had already differentiated into osteocytes or adipocytes. This discrepancy in seeding time points was necessary because each cell type required specific media, which could only be delivered through a single vascular compartment in the 3D-PBR. To improve physiological relevance, future development will need to incorporate a common media to facilitate the simultaneous culture and differentiation of all cell types, along with molecular

scale analysis such as polymerase chain reaction. Our future efforts will address these limitations and explore BM cell behavior and disorders more comprehensively using the techniques and analysis presented in this study.

Conclusion

The data presented here demonstrate that our device facilitates in situ growth and the differentiation of MSCs into various lineages and enables coculture with vascular cells. Through IHC images, we have demonstrated the 3D-PBR's ability to induce physiologically relevant cellular morphologies, surpassing conventional static culture models. Integrating cutting-edge 3D printing technologies and alternative materials into our device has propelled the evolution of the MPS beyond the constraints of PDMS-based soft-lithography, enhancing manufacturability and 3D design capability. By addressing the mentioned limitations and continuing our efforts, we envision that our techniques will enable a more accurate and comprehensive examination of various cell behaviors and disorders. This advancement is poised to contribute significantly to both basic biological research and clinical applications through the utilization of 3D-printed in vitro platforms.

Data availability

The datasets generated during and/or analyzed during the current study are available from the corresponding author on reasonable request.

Received: 13 April 2024; Accepted: 11 March 2025
Published online: 24 March 2025

References

1. Bhatia, S. N. & Ingber, D. E. Microfluidic organs-on-chips. *Nat. Biotechnol.* **32**, 760–772. https://doi.org/10.1038/nbt.2989 (2014).
2. Low, L. A., Mummery, C., Berridge, B. R., Austin, C. P. & Tagle, D. A. Organs-on-chips: Into the next decade. *Nat. Rev. Drug Discov.* **20**, 345–361. https://doi.org/10.1038/s41573-020-0079-3 (2021).
3. Richards, D., Jia, J., Yost, M., Markwald, R. & Mei, Y. 3D bioprinting for vascularized tissue fabrication. *Ann. Biomed. Eng.* **45**, 132–147. https://doi.org/10.1007/s10439-016-1653-z (2017).
4. Santos Rosalem, G. et al. Microfluidics and organ-on-a-chip technologies: A systematic review of the methods used to mimic bone marrow. *PLoS ONE* **15**, e0243840 (2020).
5. Kim, K. M. et al. Shear stress induced by an interstitial level of slow flow increases the osteogenic differentiation of mesenchymal stem cells through TAZ activation. *PLoS ONE* **9**, e92427 (2014).
6. Dallas, S. L. & Bonewald, L. F. Dynamics of the transition from osteoblast to osteocyte. *Ann. N. Y. Acad. Sci.* **1192**, 437–443 (2010).
7. Chen, Q. et al. Fate decision of mesenchymal stem cells: Adipocytes or osteoblasts?. *Cell Death Differ.* **23**, 1128–1139 (2016).
8. Gabetti, S. et al. An automated 3D-printed perfusion bioreactor combinable with pulsed electromagnetic field stimulators for bone tissue investigations. *Sci. Rep.* **12**, 13859. https://doi.org/10.1038/s41598-022-18075-1 (2022).
9. Hemmingsen, M. et al. The role of paracrine and autocrine signaling in the early phase of adipogenic differentiation of adipose-derived stem cells. *PLoS ONE* **8**, e63638 (2013).
10. Liu, Y., Kongsuphol, P., Gourikutty, S. B. N. & Ramadan, Q. Human adipocyte differentiation and characterization in a perfusion-based cell culture device. *Biomed. Microdev.* **19**, 18. https://doi.org/10.1007/s10544-017-0164-5 (2017).
11. Yamada, S. et al. Unique osteogenic profile of bone marrow stem cells stimulated in perfusion bioreactor is Rho-ROCK-mediated contractility dependent. *Bioeng. Transl. Med.* **8**, e10509 (2023).
12. Aleman, J. et al. Deconstructed microfluidic bone marrow on-a-chip to study normal and malignant hemopoietic cell-niche interactions. *Small* **15**, 1902971 (2019).
13. Bruce, A. et al. Three-dimensional microfluidic tri-culture model of the bone marrow microenvironment for study of acute lymphoblastic leukemia. *PLoS One* **10**, e0140506 (2015).
14. Carrion, B. et al. Recreating the perivascular niche ex vivo using a microfluidic approach. *Biotechnol. Bioeng.* **107**, 1020–1028 (2010).
15. Chou, D. B. et al. On-chip recapitulation of clinical bone marrow toxicities and patient-specific pathophysiology. *Nat. biomed. Eng.* **4**, 394–406 (2020).
16. Glaser, D. E. et al. Organ-on-a-chip model of vascularized human bone marrow niches. *Biomaterials* **280**, 121245 (2022).
17. Herland, A. et al. Quantitative prediction of human pharmacokinetic responses to drugs via fluidically coupled vascularized organ chips. *Nat. Biomed. Eng.* **4**, 421–436 (2020).
18. Houshmand, M. et al. Mimicking the acute myeloid leukemia niche for molecular study and drug screening. *Tissue. Eng. Part C: Method.* **23**, 72–85 (2017).
19. Kefallinou, D., Grigoriou, M., Boumpas, D. T., Gogolides, E. & Tserepi, A. Fabrication of a 3D microfluidic cell culture device for bone marrow-on-a-chip. *Micro. Nano. Eng.* **9**, 100075 (2020).
20. Marturano-Kruik, A. et al. Human bone perivascular niche-on-a-chip for studying metastatic colonization. *Proc. Natl. Acad. Sci.* **115**, 1256–1261 (2018).
21. Sieber, S. et al. Bone marrow-on-a-chip: Long-term culture of human haematopoietic stem cells in a three-dimensional microfluidic environment. *J. Tissue. Eng. Regener. Med.* **12**, 479–489. https://doi.org/10.1002/term.2507 (2018).
22. Sung, J. H., Kam, C. & Shuler, M. L. A microfluidic device for a pharmacokinetic–pharmacodynamic (PK–PD) model on a chip. *Lab. Chip.* **10**, 446–455 (2010).
23. Thon, J. N. et al. Platelet bioreactor-on-a-chip Blood. *J. Am. Soc. Hematol.* **124**, 1857–1867 (2014).
24. Torisawa, Y.-S. et al. Modeling hematopoiesis and responses to radiation countermeasures in a bone marrow-on-a-chip. *Tissue Eng. Part C: Method.* **22**, 509–515 (2016).
25. Torisawa, Y.-S. et al. Bone marrow–on–a–chip replicates hematopoietic niche physiology in vitro. *Nat. Method.* **11**, 663–669. https://doi.org/10.1038/nmeth.2938 (2014).
26. Zhang, W. et al. Ex vivo maintenance of primary human multiple myeloma cells through the optimization of the osteoblastic niche. *PLoS One* **10**, e0125995 (2015).
27. Zhang, W., Lee, W. Y., Siegel, D. S., Tolias, P. & Zilberberg, J. Patient-specific 3D microfluidic tissue model for multiple myeloma. *Tissue Eng. Part C: Method.* **20**, 663–670 (2014).
28. Zheng, Y. et al. Angiogenesis in liquid tumors: An in vitro assay for leukemic-cell-induced bone marrow angiogenesis. *Adv. Healthc. Mater.* **5**, 1014–1024 (2016).
29. McAleer, C. W. et al. Multi-organ system for the evaluation of efficacy and off-target toxicity of anticancer therapeutics. *Sci. Transl. Med.* **11**, eaav1386 (2019).
30. Miller, P. G. & Shuler, M. L. Design and demonstration of a pumpless 14 compartment microphysiological system. *Biotechnol. Bioeng.* **113**, 2213–2227 (2016).
31. Khin, Z. P. et al. A preclinical assay for chemosensitivity in multiple myeloma. *Cancer Res.* **74**, 56–67 (2014).

32. Kotha, S. S. et al. Engineering a multicellular vascular niche to model hematopoietic cell trafficking. *Stem Cell Res. Ther.* **9**, 1–14 (2018).
33. Wuchter, P. et al. Microcavity arrays as an in vitro model system of the bone marrow niche for hematopoietic stem cells. *Cell Tissue res.* **364**, 573–584 (2016).
34. Sung, J. H. & Shuler, M. L. A micro cell culture analog (μCCA) with 3-D hydrogel culture of multiple cell lines to assess metabolism-dependent cytotoxicity of anti-cancer drugs. *Lab. Chip.* **9**, 1385–1394 (2009).
35. Piard, C. et al. 3D printed HUVECs/MSCs cocultures impact cellular interactions and angiogenesis depending on cell-cell distance. *Biomaterials* **222**, 119423 (2019).
36. Joshi, A. et al. Co-culture of mesenchymal stem cells and human umbilical vein endothelial cells on heparinized polycaprolactone/gelatin co-spun nanofibers for improved endothelium remodeling. *Int. J. Biol.macromol.* **151**, 186–192 (2020).
37. Bhattacharjee, N., Urrios, A., Kang, S. & Folch, A. The upcoming 3D-printing revolution in microfluidics. *Lab. Chip.* **16**, 1720–1742 (2016).
38. Pitzanti, G. et al. Urethane dimethacrylate-based photopolymerizable resins for stereolithography 3D printing: A physicochemical characterisation and biocompatibility evaluation. *Drug Deliv. Transl. Res.* **14**, 177–190 (2024).
39. Rodrigues, P. M., Xavier, M., Calero, V., Pastrana, L. & Gonçalves, C. Partitioning of small hydrophobic molecules into polydimethylsiloxane in microfluidic analytical devices. *Micromachines* **13**, 713 (2022).
40. Tanaka, J., Hashimoto, T., Stansbury, J. W., Antonucci, J. M. & Suzuki, K. Polymer properties on resins composed of UDMA and methacrylates with the carboxyl group. *Dent. Mater. J.* **20**, 206–215 (2001).
41. van Meer, B. J. et al. Small molecule absorption by PDMS in the context of drug response bioassays. *Biochem. Biophys. Res. Commun.* **482**, 323–328. https://doi.org/10.1016/j.bbrc.2016.11.062 (2017).
42. Wang, J. D., Douville, N. J., Takayama, S. & ElSayed, M. Quantitative analysis of molecular absorption into PDMS microfluidic channels. *Ann. Biomed. Eng.* **40**, 1862–1873. https://doi.org/10.1007/s10439-012-0562-z (2012).
43. Panek, M. et al. Bone tissue engineering in a perfusion bioreactor using Dexamethasone-loaded peptide hydrogel. *Materials (Basel)* https://doi.org/10.3390/ma12060919 (2019).
44. Jun, B. H., Ahmadzadegan, A., Ardekani, A. M., Solorio, L. & Vlachos, P. P. Multi-feature-Based Robust Cell Tracking. *Ann. Biom. Eng.* **51**, 604–617. https://doi.org/10.1007/s10439-022-03073-1 (2023).
45. Jun, B. H. et al. Fibronectin-expressing mesenchymal tumor cells promote breast cancer metastasis. *Cancers* **12**, 2553 (2020).
46. Vasilevich, A. S. et al. On the correlation between material-induced cell shape and phenotypical response of human mesenchymal stem cells. *Sci. Rep.* **10**, 18988. https://doi.org/10.1038/s41598-020-76019-z (2020).
47. Wirth, M. A. Shape analysis and measurement. *Image Process. Gr.* 1–49 (2004).
48. Fakhry, M., Hamade, E., Badran, B., Buchet, R. & Magne, D. Molecular mechanisms of mesenchymal stem cell differentiation towards osteoblasts. *World J. Stem. Cell.* **5**, 136–148. https://doi.org/10.4252/wjsc.v5.i4.136 (2013).
49. Skottke, J., Gelinsky, M. & Bernhardt, A. In vitro co-culture model of primary human osteoblasts and osteocytes in collagen gels. *Int. J. Mol. Sci.* **20**, 1998 (2019).
50. Compera, N. et al. Adipose microtissue-on-chip: A 3D cell culture platform for differentiation, stimulation, and proteomic analysis of human adipocytes. *Lab. Chip.* **22**, 3172–3186 (2022).

Acknowledgements

The authors would like to acknowledge Leyla Akh for assisting with the equipment training. Research presented in this article was supported by the Laboratory Directed Research and Development program of Los Alamos National Laboratory under project number LDRD20210204DR. Figure 2 and Figure 6 illustrations were created with BioRender.com.

Author contributions

Conceptualization, D.J.R., J.F.H., and K.L.D.; methodology, B.H.J., J.E.T., D.J.R., J.F.H., and K.L.D.; investigation, B.H.J., J.E.T., D.J.R., B.M.P., M.O.I., A.M.R., J.F.H., and K.L.D.; resources, D.J.R., M.O.I., J.F.H., and K.L.D.; Fabrication, B.H.J., J.E.T., D.J.R., and M.O.I.; Visualization, B.H.J.; formal analysis, B.H.J.; writing—original draft preparation, B.H.J.; writing—review and editing, B.H.J., J.E.T., D.J.R., B.M.P., M.O.I., A.M.R., J.F.H., and K.L.D.; supervision, J.F.H., and K.L.D.; project administration, B.H.J., J.F.H., and K.L.D.; funding acquisition, J.F.H., and K.L.D.; All authors have read and agreed to the current version of the manuscript.

Declarations

Competing interests

The authors declare no competing interest.

Additional information

Correspondence and requests for materials should be addressed to K.L.D.-A.

Reprints and permissions information is available at www.nature.com/reprints.

Publisher's note Springer Nature remains neutral with regard to jurisdictional claims in published maps and institutional affiliations.